AGU PUBLICATIONS

Geochemistry, Geophysics, Geosystems

RESEARCH ARTICLE
10.1002/2016GC006443

Horizontal compressive stress regime on the northern Cascadia margin inferred from borehole breakouts

M. Riedel[1], A. Malinverno[2], K. Wang[3], D. Goldberg[2], and G. Guerin[2]

[1]GEOMAR Helmholtz Centre for Ocean Research Kiel, Marine Geodynamics, Kiel, Germany, [2]Lamont Doherty Earth Observatory of Columbia University, Palisades, New York, USA, [3]Geological Survey of Canada, Sidney, British Columbia, Canada

Key Points:
- Logging-while-drilling and wireline data at the northern Cascadia margin are used to measure breakout orientations
- Maximum horizontal compressive stress S_{Hmax} is generally margin-normal and consistent with plate convergence
- If S_{Hmax} is greater than the vertical stress, a margin-normal S_{Hmax} is consistent with locking of a velocity-weakening megathrust

Correspondence to:
M. Riedel,
mriedel@geomar.de

Citation:
Riedel, M., A. Malinverno, K. Wang, D. Goldberg, and G. Guerin (2016), Horizontal compressive stress regime on the northern Cascadia margin inferred from borehole breakouts, *Geochem. Geophys. Geosyst.*, *17*, doi:10.1002/2016GC006443.

Received 18 MAY 2016
Accepted 11 AUG 2016
Accepted article online 17 AUG 2016

Abstract During Integrated Ocean Drilling Program Expedition 311 five boreholes were drilled across the accretionary prism of the northern Cascadia subduction zone. Logging-while-drilling borehole images are utilized to determine breakout orientations to define maximum horizontal compressive stress orientations. Additionally, wireline logging data at two of these sites and from Site 889 of Ocean Drilling Program Leg 146 are used to define breakouts from differences in the aperture of caliper arms. At most sites, the maximum horizontal compressive stress S_{Hmax} is margin-normal, consistent with plate convergence. Deviations from this trend reflect local structural perturbations. Our results do not constrain stress magnitudes. If the margin-normal compressional stress is greater than the vertical stress, the margin-normal S_{Hmax} direction we observe may reflect current locking of a velocity-weakening shallow megathrust and thus potential for trench-breaching, tsunamigenic rupture in a future megathrust earthquake.

1. Introduction

Convergent margins, such as the Cascadia subduction zone, host some of the largest earthquakes, often accompanied by devastating tsunamis such as the Sumatra-Andaman 2004 earthquake [*Lay et al*., 2005; *Rabinovich and Thomson*, 2007] and the Tohoku-Oki 2011 earthquake [*Kodaira et al*., 2012; *Tajima et al*., 2013]. Understanding the mechanisms of earthquake generation, recurrence pattern, and potential for tsunami generation is important to hazard assessment and risk mitigation. Constraining the state of stress in the accretionary complex of the overriding plate is a key element in developing such understanding. The state of stress within the accretionary prism generally is controlled by the mechanical coupling at the interface between downgoing and overriding plates and by gravity [e.g., *Wang and Hu*, 2006; *Wang and He*, 2008]. Although the maximum stress direction in the prism is thought to be associated with compression due to shear traction along the subduction megathrust [*Zoback*, 1992], deviations from this general pattern are important to detect, as they help to understand stress-fluctuations during earthquake cycles.

The state of intraslab stress at the Cascadia subduction zone has been defined previously from inversion of earthquake focal mechanisms [*Wada et al*., 2010]. In northern Cascadia the Juan de Fuca slab is primarily under compression normal to the slab surface with tension in the downdip direction as a result of the overall net slab pull. As proposed by *Wang et al*. [1997], vector combination of the net slab pull and subduction resistance results in a right-lateral shear traction acting on the surface portion of the Juan de Fuca plate along most part of the subduction boundary, but the traction is margin-normal or even left-lateral off Vancouver Island.

We report new observations of the state of stress within the upper ~300 m below seafloor (mbsf) of the accretionary prism at the northern Cascadia margin as defined from borehole breakouts and fracture alignments. Breakouts record the present state of stress, and fracture alignments depend on the stress state at the time of fracture formation. The breakouts are based on logging data from Integrated Ocean Drilling Program (IODP) Expedition 311 in 2005 [*Riedel et al*., 2006] and Ocean Drilling Program (ODP) Leg 146 in 1992 [*Westbrook et al*., 1994] and are compared to fault trends identified from seafloor multibeam bathymetry and seismic data. Focal mechanisms of crustal earthquakes [e.g., *Wang et al*., 1995; *Balfour et al*., 2011] provide additional constraint on the state of stress in the broader region.

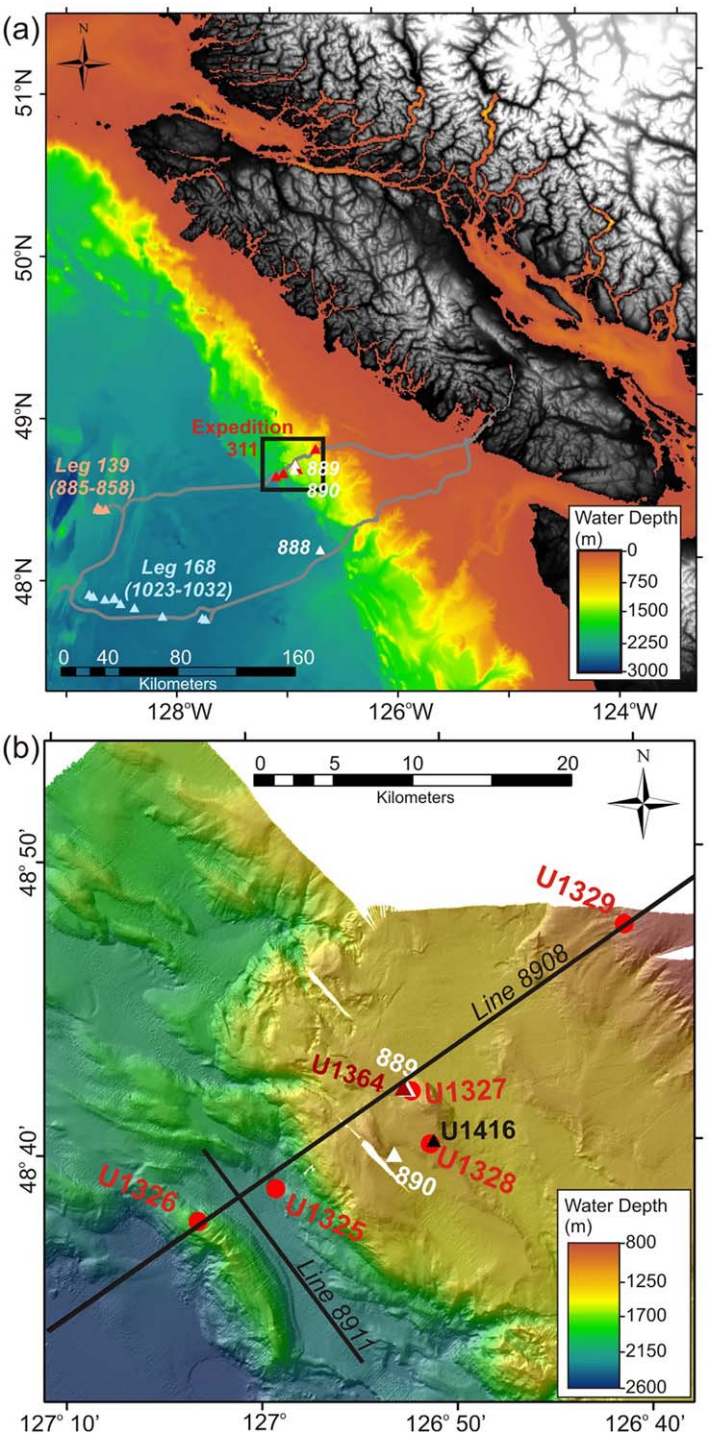

Figure 1. (a) Map showing northern Cascadia margin with locations of IODP Expedition 311 (X311) transect (red triangles), as well as other drilling studies on the Cascadia margin from ODP Leg 146 (white triangles) and Legs 139 and Leg 168. The cabled observatory NEPTUNE operated by Ocean Networks Canada is shown as gray line. (b) Detailed view of the X311 transect, including locations of borehole observatories from IODP Expeditions 328 (U1364) and 346S (U1416). Multichannel seismic lines 8908 (Figure 2) and 8911 (Figure 9b) are indicated by black lines (see Figure 2).

Borehole breakouts have previously been successfully used to define stress orientations in central Cascadia at Southern Hydrate Ridge off Oregon [*Goldberg and Janik*, 2006], and in other subduction zone settings such as off Costa Rica as part of the IODP CRISP project [*Malinverno et al*., 2016], at the Nankai trough as part of the IODP NanTroSEIZE project [*Lin et al*., 2010; *Chang et al*., 2010] and ODP Leg 196 [*McNeill et al*., 2004], and at the Japan Trench as part of the IODP J-FAST project [*Lin et al*., 2013].

2. Geological Background

At the Cascadia subduction zone, the Juan de Fuca plate is subducting beneath the North American plate (Figure 1) at a rate of ~46 mm/yr with a relative motion direction of ~49° [*DeMets et al*., 2010]. In northern Cascadia the oceanic plate is young (2–6 Ma) and therefore warm and buoyant [*Davis et al*., 1990]. The 1 to 2 km thick sedimentary section that lies on top of the oceanic plate near the deformation front consists of a mix of fine-grained hemi-pelagic sediments and coarser-grained turbidites [*Westbrook et al*., 1994]. At the deformation front, the sediment is mostly scraped off and accreted to the margin [*Davis and Hyndman*, 1989] resulting in a large accretionary prism hosting a series of ridges and folds. The accretion of sediments leads to overall sediment thickening and bulk shortening as well as fluid expulsion [*Hyndman et al*., 1993; *Hyndman et al*., 2001]. The upwardly expelled fluids are rich in methane, and as a consequence, gas hydrate occurs across the prism from the deformation front to the eastward limit of regional gas hydrate occurrence in water depths of ~900 m [e.g., *Riedel et al*., 2010]. Several boreholes have been drilled off Vancouver Island during ODP Leg 146 and IODP Expedition 311,

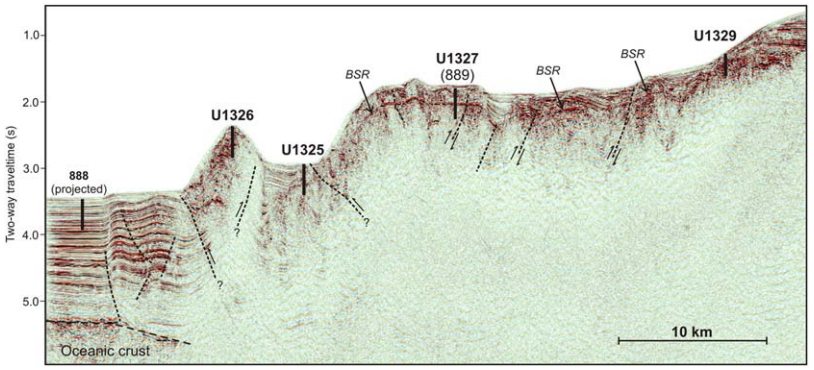

Figure 2. Section of seismic line 8908 along the IODP Expedition 311 drilling transect showing location of boreholes as well as main faults (black dashed lines). The margin-wide bottom-simulating reflector (BSR) is indicated by black arrows.

which document gas hydrate settings and associated sedimentology [e.g., *Westbrook et al*., 1994; *Kastner et al*., 1995; *Malinverno et al*., 2008; *Torres et al*., 2008; *Riedel et al*., 2010]. Most drill sites are along a central seismic line (Figure 2) across the accretionary wedge. Numerous additional studies incorporating seismic data, geological sampling, heat flow measurements, and long-term observations have been conducted to further understand the gas hydrate occurrence, origin of methane, and fluid-flux regime across the prism [e.g., *Hyndman and Davis*, 1992; *Yuan et al*., 1999; *Riedel et al*., 2009]. The geological and geophysical observations from these studies have provided valuable background information for our study of the stress field.

3. Methodology and Data

Following previous analyses of breakout detection [e.g., *Goldberg and Janik*, 2006; *Malinverno et al*., 2016], we utilize the logging-while-drilling (LWD) 360°-coverage borehole images of the electrical resistivity at bit (RAB) and bulk density from all five sites drilled during IODP Expedition 311 (U1325-U1329). The vertical resolution of the LWD data is limited by the rate of penetration (~25 m/h on average during X311) during data acquisition and an effective vertical sampling resolution of ~0.25 m was achieved. The LWD image data were first processed to incorporate magnetic declination and then rotated according to the azimuthal reference. Log processing details (and further information on drilling parameters such as rate of penetration) can be found as part of the processing notes provided online at the IODP logging database (e.g., http://brg.ldeo.columbia.edu/data/iodp-usio/exp311/U1328C/documents/index_documents.html) or the X311 Proceedings [*Riedel et al*., 2006]. The X311 Proceedings describe the overall logging results, but the analysis of breakout orientations that we present here is new.

Borehole breakout results are usually interpreted in terms of three stress components: the vertical stress (S_V), the maximum (most compressive) horizontal stress S_{Hmax}, and the minimum horizontal stress S_{hmin}. If the state of stress is Andersonian, these will be the three principal stresses. Drilling a borehole into a formation exposed to differential horizontal stresses ($S_{Hmax} > S_{hmin}$) induces a circumferential stress around the borehole wall that reaches a compressive maximum at the azimuth of S_{hmin}. If the circumferential stress exceeds the rock strength, the borehole wall will spall and develop characteristic breakouts on opposite sides of the borehole as depicted in Figure 3 [*Zoback et al*., 2003]. In LWD image data, borehole breakouts appear as vertical zones of lower electrical resistivity and bulk density due to the larger fluid-filled gap between the tool sensors and the borehole wall. We interpreted the unwrapped LWD image data for borehole breakouts and fracture alignments following the guidelines provided by the World Stress Map Project [*Tingay et al*., 2008]. We recorded the depth and azimuth of individual breakouts and combined RAB and density image information for final determination of the azimuth of S_{hmin}. The average azimuth of S_{Hmax} with a standard deviation is reported for each borehole. Downhole changes of S_{Hmax} can also be exploited to detect lithology or structurally driven variations in the stress regime.

Wireline logging measurements indicate the presence of borehole breakouts by the aperture and orientation of the arms of a four-arm caliper tool, such as the Formation MicroScanner (FMS). As these tools are pulled uphole, they normally rotate due to cable torque. When breakouts are present, one opposing pair of

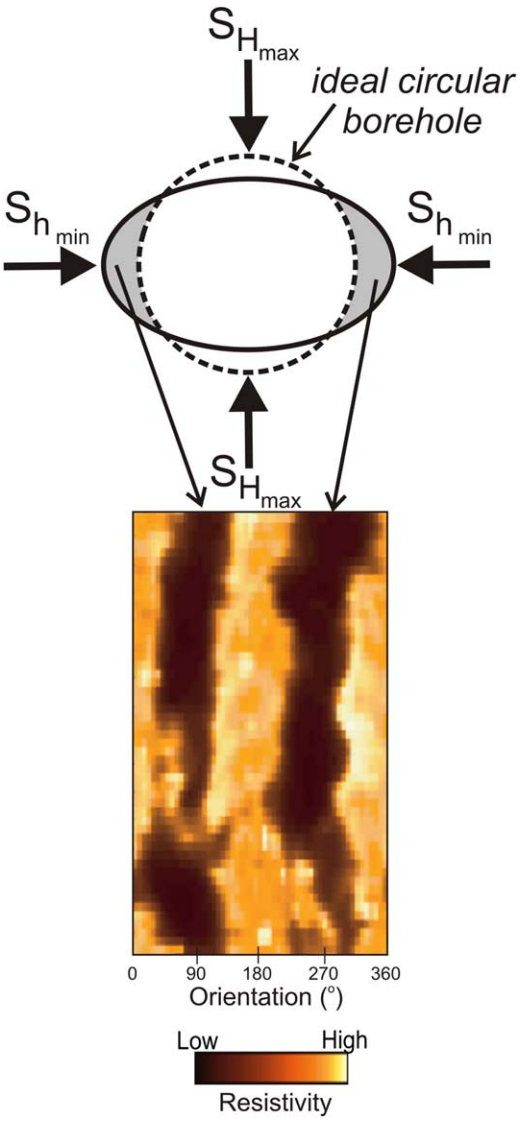

Figure 3. Schematic diagram illustrating the effect of differential stresses on an idealized borehole and resulting breakouts (gray shaded regions). The maximum compressive stress (S_{Hmax}) squeezes the borehole, deforming it into an ellipse. The generic example of unwrapped LWD borehole imagery depicts then two stripes of reduced electrical resistivity indicating zones of the enlarged borehole, where the LWD tool lost contact to the borehole wall (modified from *Goldberg and Janik* [2006]).

the caliper arms tends to remain set into the enlargement along a particular azimuth of the hole [*Bell and Gough*, 1979; *Plumb and Hickman*, 1985; *Lin et al*., 2010]. Thus, breakouts can be detected when the difference in the orthogonal borehole radii is significant and consistent in orientation over an interval. *Bell and Gough* [1979] first discovered breakouts in numerous oil and gas wells in Alberta, Canada using this method. We identify breakouts in the Cascadia data where caliper anomalies show differences greater than 1.2 inches (3.05 cm).

4. Results of Breakout Analyses

4.1. General Observations

Figure 4 shows a summary of the RAB data used for our breakout analyses combined with the main lithological units identified at the five X311 drill sites. The breakouts are continuous through most of the logged intervals at all sites, crossing lithological boundaries and the gas hydrate stability zone, and indicate a rather uniform stress field across the transect. A comparison of breakouts observed in the wireline FMS caliper logs with the LWD borehole image data is shown in Figure 5. The locations and azimuths of the breakouts are very similar between the two data sets. Combining all the breakout information observed in LWD and FMS caliper data, histograms of the azimuthal distributions (rose diagrams) show consistent downhole trends in orientation with relatively small standard deviation at all sites (Figure 6). All breakout-inferred orientations of S_{Hmax} are listed in Table 1. With the exception of Site U1325, all sites indicate NE-SW trending S_{Hmax}. Site U1325 is different in having a S_{Hmax} oriented approximately E-W.

4.2. Site U1326

Site U1326 was drilled close to the deformation front into a ridge that is characterized by a large slope failure and numerous normal faults perpendicular to the main axis of the accretionary ridge [*Lopez et al*., 2010; *Hamilton et al*., 2015]. The axis of the accretionary ridge trends nominally NW-SE, but bends progressively from N to S, causing an overall concave southwestward shape of the ridge (Figure 7).

Breakouts at Hole U1326A (Figure 6a) drilled at the northern edge of the ridge suggest a compressive regime that aligns with the orientation of the local ridge axis (Figure 7). The borehole data also show numerous dipping bedding planes throughout the drilled interval. These planes consistently dip at $>70°$ in the direction of $\sim 45°$ (NE), i.e., striking 315°. This strike direction matches the strike of sediment layers imaged by seismic sections across this ridge (Figures 8a and 8b). The sediments, initially deposited on the abyssal plain, were progressively folded and thrusted upward to form the ridge. Three lithostratigraphic units were defined at Site U1326, although the entire cored interval is relatively homogenous in the occurrence of dominantly fine-grained sediments (clay to silty clay) with interspersed coarse-grained silty/sandy turbidites [*Riedel et al*., 2006]. Lithostratigraphic Units I and II were divided based on abundant soft-

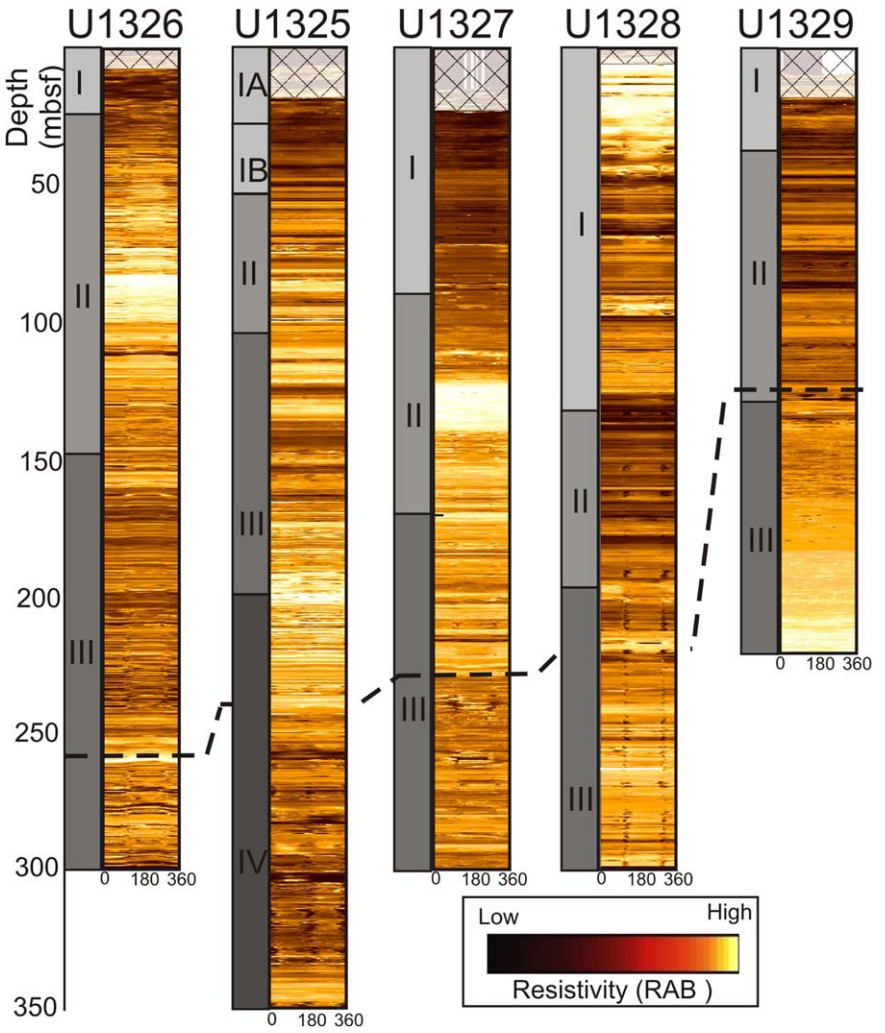

Figure 4. Summary of logging-while-drilling (LWD) deep-button resistivity at bit (RAB) images from all sites of IODP Expedition 311. Data are shown from left to right following the drilling transect from the western Site U1326 drilled into the frontal ridge at the deformation front, to the eastern-most Site U1329. The black dashed line represents the base of the gas hydrate stability zone [*Riedel et al*., 2010]. To the left of each RAB-image the lithostratigraphic units are shown [*Riedel et al*., 2006]. Breakouts are seen across all units as well as above and below the gas hydrate stability zone. The uppermost 5–15 m of LWD data at all sites are degraded because of an enlarged hole near the seafloor and are not used in this analysis. Each unwrapped RAB image covers the 360° range of the borehole wall.

sediment deformation and dipping strata as well as occurrences of biogenic components beneath ~34 mbsf. Lithostratigraphic Unit III shows fewer turbidite input and is marked by an onset of diatoms at ~146 mbsf. Unit III is overall composed of 37% diatoms. Hole U1326A intersects the ridge slightly east of the apex of the anticline, generating an apparent north-easterly dip of sediment layers. Normal faults were observed in the core from Hole U1326A (e.g., core interval U1326C-6X-5, 16–35 cm, Figure 8a) which suggests that pervasive structural deformation of these sediments occurred after deposition. Breakouts were observed across all lithological units as well as above and below the gas hydrate stability zone (GHSZ) with no change in orientation. The direction of maximum horizontal compression (S_{Hmax}) is ~30° and almost perpendicular to the strike of the frontal ridge segment north of the prominent slope failure (Figure 7).

4.3. Site U1325

Site U1325 is located further along the X311 drilling transect ~5 km landward of the deformation front. The site is within a slope basin where sediments are affected by a buried ridge of accreted sediments that does not crop out on the seafloor (Figure 9a). The resulting uplift of the ridge caused syn-depositional tilting of the slope-basin sediments.

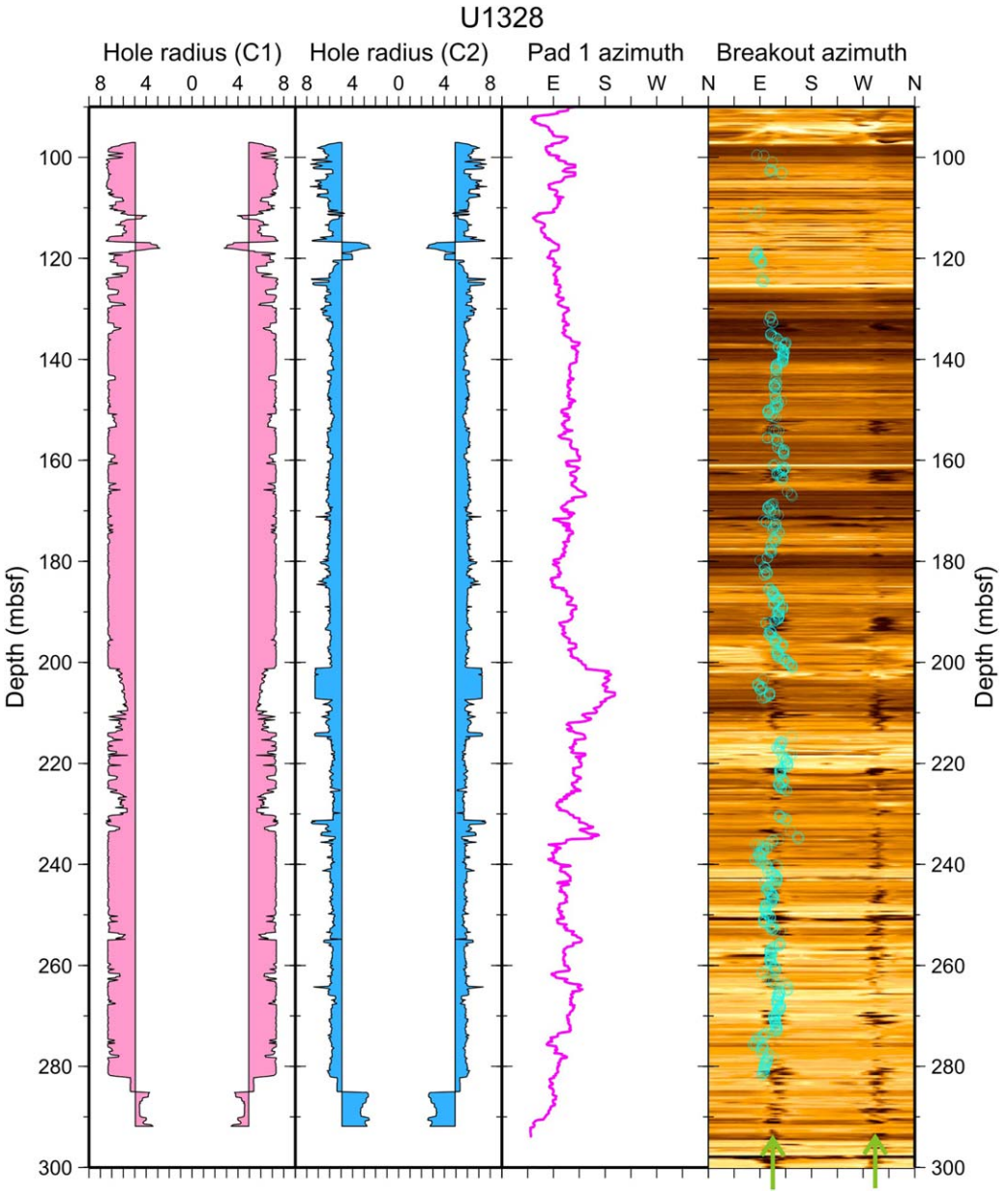

Figure 5. Example of the wireline-derived breakout orientations compared to the logging-while-drilling (LWD) borehole image at Site U1328 (Bullseye Vent). The borehole radius (Hole U1328C, drilled approximately 40 m to the SW of Hole U1328A) shown in the two left columns, combined with the formation micro scanner (FMS) data yields breakout orientations that are overlain as circles onto the LWD image (right most column) measured in Hole U1328A. Note, only one quadrant of the wireline derived breakouts is shown for clearer comparison of the LWD and wireline results. The nearly vertical lines of low resistivity patches seen on the LWD image are indicated by the green arrows.

Four lithostratigraphic units were defined at Site U1325. The entire 350 m of recovered core are dominantly fine grained detrital sediment (clay to silty clay) with interspersed coarse-grained turbidites [*Riedel et al.*, 2006]. Units I–III were distinguished by the sudden absence of diatoms in Unit II (from ~52 to 102 mbsf). In contrast, Unit III has again a high abundance of biogenic components (up to 50%). Unit IV (198–350 mbsf) is characterized by both low turbidite input and an absence of biogenic components. Most breakouts (~80%) appear below 232 mbsf within lithologic Unit IV (Figure 4), but without any change in orientation relative to the breakouts observed above.

At this site, the orientation of S_{Hmax} derived from the borehole breakouts is almost E-W (~98°), parallel to the strike of nearby accretionary ridges that outcrop slightly north of the drill site. Site U1325 is part of a basin that develops between two major thrust fault systems to the west giving rise to the ridge of Site

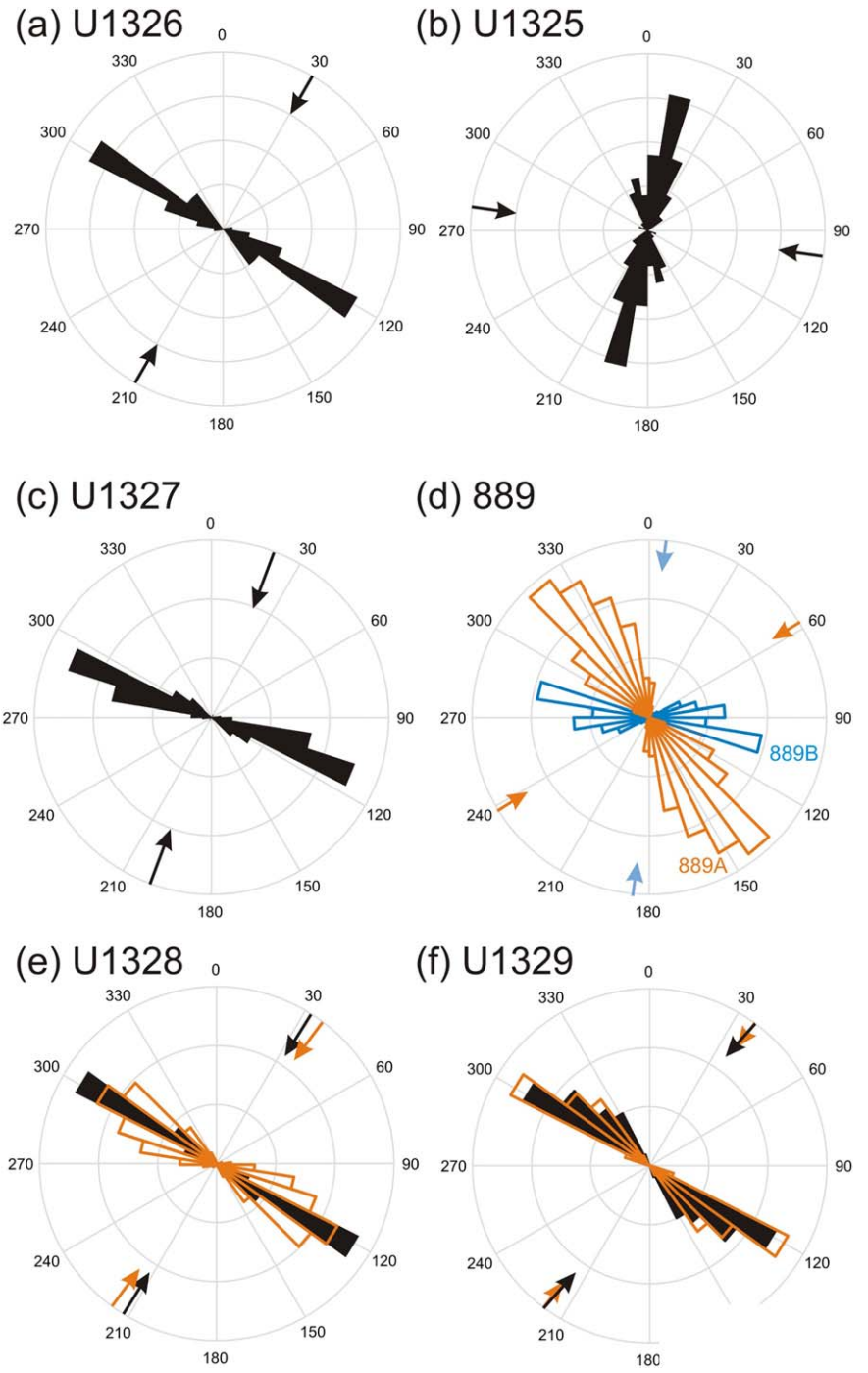

Figure 6. Summary of all breakout data from LWD (black) and wireline log data (orange, blue) at all sites on the northern Cascadia margin. The corresponding values of S_{Hmax} and standard deviations) are summarized in Table 1. Arrows are orientations of S_{Hmax}.

U1326 and the east where Sites U1327, U1328, and 889 are located. Subsidence in response to the thrust faults and continuous sedimentation of turbidites and hemipelagic mud has filled up to 800 m in this well-layered slope basin, which is wedged between secondary buried ridges resulting in progressive tilting of the sediment layers (Figure 9).

4.4. Sites U1327 and 889

Sites U1327 and 889 are located at the midpoint of the drilling transect, ~20 km east of the deformation front. The drill holes are near two prominent topographic highs that rise >200 m above the surrounding

Table 1. Average Orientations and Standard Deviations (°) of S_{Hmax} From Breakouts Observed With LWD and Wireline Data

Site/Hole	S_{Hmax} LWD Breakouts	S_{Hmax} Wireline Breakouts
U1325	98.0 ±17.7	n.d.
U1326	29.8 ± 13.9	n.d.
U1327	20.5 ± 7.6	n.d.
889A	n.d.	58.6 ± 18.7
889B	n.d.	8.1 ± 23.7
U1328	32.0 ± 5.9	27.8 ± 15.3
U1329	41.7 ± 10.8	36.5 ± 10.1

seafloor (Figure 10). Sediments at Site U1327 were divided into three lithostratigraphic units [*Riedel et al.*, 2006]. The lithostratigraphic boundary between Units I (slope-basin sediments) and II (accreted sediments) at a depth of ~90 mbsf is marked by a sharp decrease in the number and thickness of sand and silt layers and the onset of diatom-rich sediments. The top of lithostratigraphic Unit III is defined at a depth of ~170 mbsf based on the sudden absence of diatoms and a high degree of induration of the sediments. Breakouts were observed from LWD data in Hole U1327A over an interval from 36 to 300 mbsf, crossing all lithologic units and the GHSZ with no significant change in orientation. No wireline FMS data were acquired at Site U1327. Two passes of wireline FMS data each were acquired in Hole 889A (from 80 to 260 mbsf) and Hole 889B (from 100 to 250 mbsf). Breakouts from the wireline data in both holes are observed below a depth of 84 mbsf, within the accreted sediments only.

Data from Site U1327 yield an orientation of S_{Hmax} of 20.5° with little variation (±8° standard deviation). Data from Holes 889A and 889B indicate S_{Hmax} orientations that vary from ~59° (±19°) at Hole 889A to ~8° (±24°) at Hole 889B (Figure 6). The S_{Hmax} directions inferred from wireline data in the two Site 889 boreholes drilled during ODP Leg 146 have much larger standard deviations than the LWD data.

These three boreholes lie within a region of dense seismic data coverage acquired for ODP Leg 146 and X311 predrilling site surveys. We have mapped the extent of the boundary between slope-basin sediments and the underlying accreted material as an indicator of the main structural features and underlying tectonics (Figure 10). The accreted sediments (acoustically more chaotic to transparent in character, Figure 11) form a prominent ridge east of the drill sites (Figure 10). A prominent thrust fault is located east of the ridge [*Westbrook et al.*, 1994] and numerous smaller normal and strike-slip faults, partially associated with cold vent activity, were identified [*Furlong*, 2013; *Riedel et al.*, 2010; *Paull et al.*, 2015] resulting in a complex fault pattern overall around these boreholes.

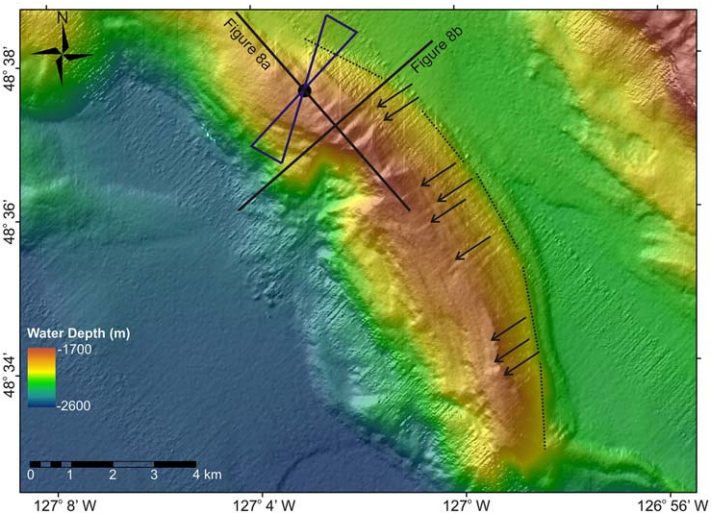

Figure 7. Results of breakout analyses at Site U1326 at the frontal deformation front compared to the bathymetry around the drill site. The breakouts reflect the main compression that gave rise to the NW-portion of the frontal ridge. Further south along the ridge, the crest of the anticline strikes N-S. The rotation of the strike direction is indicated by the short dotted line segments. Normal faults (indicated by black arrows) cut the frontal ridge in a dominant SW-NE orientation suggesting extension of the ridge, likely a result of gravitational collapse as previously suggested by *Lopez et al.*, [2010]. A prominent submarine slope failure is located at the central portion of the ridge [see, e.g., also *Hamilton et al.* [2015] and *Scholz et al.* [2011]). The locations of the seismic lines depicted in Figure 8 are shown by thick black lines.

4.5. Site U1328

Site U1328 (Bullseye Vent), located ~3.5 km south of U1327, intersected laminated slope-basin sediments deposited in a minibasin that developed between two buried ridges of accreted sediments (Figure 12). The sediment layering shows an increasing deflection (tilt) toward the bottom of the basin. Three lithostratigraphic units were defined at Site U1328 [*Riedel et al.*, 2006]. Similar to Site U1325 and U1326, all three units consist of a mix of fine-grained sediments (clay and silty clay) with interspersed layers of coarser grained material (turbidites). The boundary between Units I and II at a depth of ~132 mbsf is marked by the onset of diatom-rich sediments in Unit II. Below ~197 mbsf, Unit III contains fewer turbidites and is

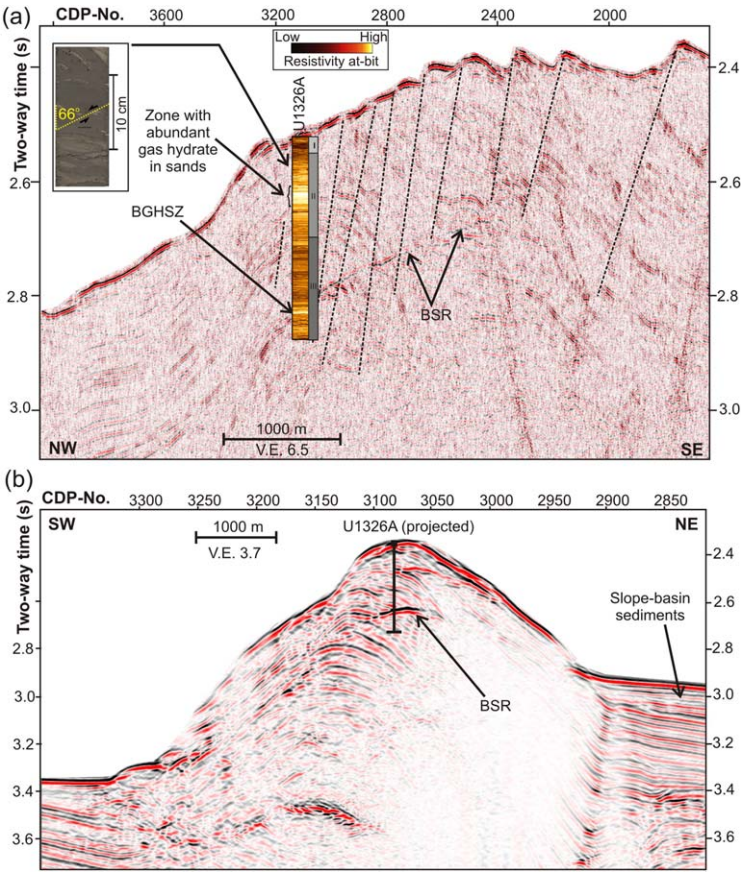

Figure 8. Seismic data around Site U1326. (a) Section of a seismic line along the ridge axis. Superimposed on the seismic line are the locations of normal faults (dashed lines) as well as the LWD resistivity data indicating the occurrence of gas hydrates in form of high resistivity values as well as dominant lithological units [*Riedel et al.*, 2006]. A bottom-simulating reflector (BSR) marking the base of the gas hydrate stability zone is seen along the section. A core sample taken at ~45 m below seafloor (Core U1326C-6X-5) shows a prominent normal fault, suggesting pervasive sediment deformation on all scales. (b) Section of seismic line 8908 crossing the ridge perpendicular to the ridge-axis. The BSR is seen beneath the crest of the ridge. The drill Site U1326 is located at the top of the ridge, but the apex of the fold-structure is further to the west, thus creating the dip-direction of sedimentary layers observed in the log data.

mostly barren of diatoms. The uppermost 40–50 mbsf of this hole is characterized by the presence of massive gas hydrate layers. Gas hydrate was also recovered in low concentrations (<5% of the pore space) below this depth. Breakouts were observed in the LWD image data from a depth of 30–298 mbsf. Two passes of wireline FMS logs in Hole U1328C show consistent breakouts orientations from ~100 to 290 mbsf across all lithostratigraphic units and above and below the GHSZ. Using the breakout orientation, the mean S_{Hmax} direction is ~32° (LWD) and ~28° (wireline, Table 1). The orientation of S_{Hmax} at this Site is consistent with the alignment of the buried accretionary ridges (Figure 12) and the shape of the basin (as outlined in Figure 10 from the isobaths of the top of accreted material).

4.6. Site U1329

The easternmost Site U1329 drilled during X311 intersected a regional unconformity at a depth of ~135 mbsf. The base of the GHSZ is located at 125 mbsf, although no gas hydrates were recovered and the BSR is only weakly developed at this site (Figure 13). Approximately ~4.5 Ma of sediments are missing from the sedimentary record at the unconformity [*Akiba et al.*, 2009]. Three lithostratigraphic units were defined at Site U1329 [*Riedel et al.*, 2006]. Lithologic Units I and II are dominated by fine-grained detrital sediments (clay to silty clay) and distinguished by the presence of diatomaceous ooze and high biogenic silica content below ~37 mbsf. Unit III contains few occurrences of coarse-grained material and has a very low sedimentation rate [*Akiba et al.*, 2009]. The lowermost part of Unit III is marked by the occurrence of a breccia, possibly representing a debris flow. Overall, the most striking feature of this site is the strong decrease in porosity and increase in electrical resistivity beneath ~170 mbsf (see Figure 4). Breakouts were observed at this Site in the LWD image-data and wireline FMS data. LWD breakouts occur from 42 to 118 mbsf and wireline breakouts are observed with a consistent orientation from 82 to 162 mbsf. S_{Hmax} directions have a mean value of ~42° from the LWD breakouts and 36.5° from wireline breakouts (Table 1). Below ~170 mbsf, the diameter of Hole U1329D becomes much smaller and a second pass of the wireline FMS could not be acquired.

5. Discussion

5.1. Impact of Sedimentological Variation and Gas Hydrate Occurrence

Breakout directions observed in our borehole images are remarkably consistent over the drilled intervals at each site, and results from LWD and wireline operations match well overall. Despite differences in the

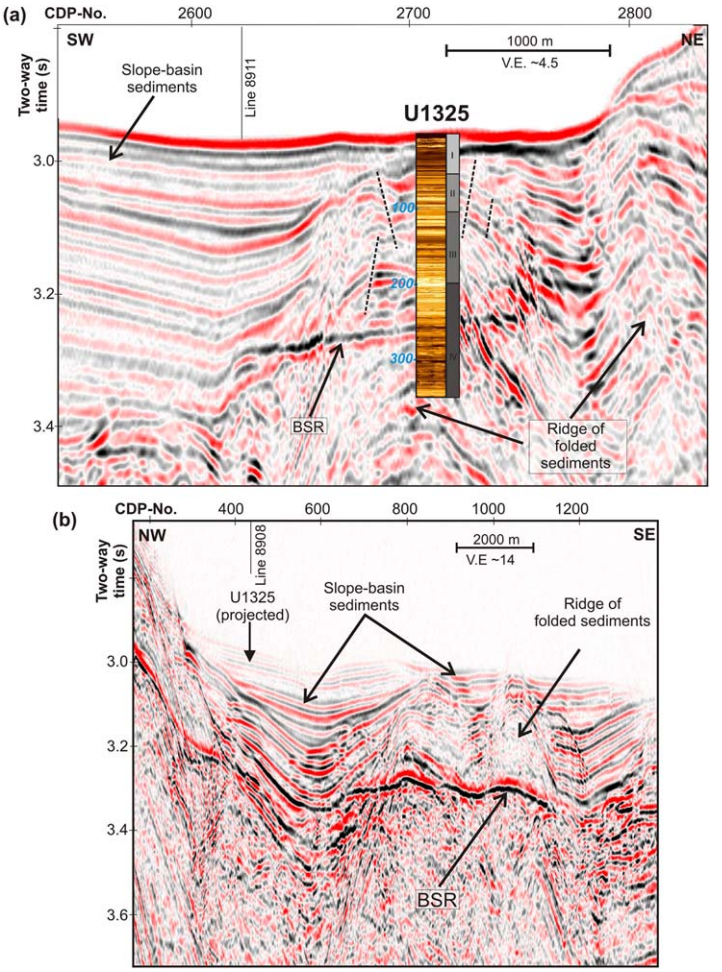

Figure 9. (a) Seismic data from MCS line 8908 at Site U1325. To the SW of the site, a slope basin is developed with a thick section of well-laminated sediments. Toward the NE, the sediments drape a ridge of highly folded sediments and are progressively deformed. A BSR is well developed at the drill site, but appears absent in the basin located to the SW. Superimposed on the seismic data are the LWD resistivity data (Figure 4) and lithostratigraphic units from X311 coring. (b) Seismic data from MCS line 8911, crossing line 8908 perpendicular, ~1 km further west of the drill site. This line clearly shows the slope-basin being wedged in between anticlinal ridges to the NW and SE of the drill site.

sediment composition at each drill site (e.g., abundance of coarse-grained silt/sand turbidites) breakout orientations appear unaltered by these changes within the statistical spread and resolution of the individual data sets. Overall, the majority of the boreholes intersect slope-basin sediments of $<$0.5 Ma of age. Only at Sites U1327 and 889 the boreholes intersect the seismically observed boundary between slope- and older accreted sediments. These older sediments, though similar in composition to the slope-basin sediments, are more indurated [*Riedel et al*., 2006] and exhibit a scaly fabric in cores from Site 889 [*Westbrook et al*., 1994]. The only minor mineralogical change noted was the occurrence of glauconite within the accreted sediments [*Westbrook et al*., 1994], which is otherwise not present in the sedimentological record cored. No change in borehole breakout orientation or abundance of breakouts is observed at Site U1327 or 889, indicating that the stress orientation at these boreholes is uniform across major lithological and stratigraphic boundaries. The oldest sediments (~6.8 Ma) were drilled and cored at Site U1329. Breakouts from the LWD data at Site U1329 are confined to the upper 125 mbsf and do not occur beneath the unconformity seen at ~135 mbsf. The wireline log data, however, did reveal breakouts beneath the unconformity at the same orientation than the breakouts above. This again shows that even at this eastern-most site the stress regime is consistent across the entire depth interval drilled and is unaffected by the presence of the unconformity.

Additionally, breakout orientation within the GHSZ is consistently observed with the same mean value as below the base of GHSZ. The overall concentration of gas hydrate within the pore-space at individual drill sites is rather low and averages ~5% [*Riedel et al*., 2010]. *Torres et al*. [2008] observe that concentrations may locally exceed 80%, especially in the coarser-grained turbidites. As such individual coarser-grained units are relatively thin, having a maximum thickness of 8–10 cm, we observe no significant impact on the shear strength of the sediment and no change in the borehole image data. For example, breakouts are consistent over the interval from 80 to 100 mbsf at Site U1326 where abundant turbidites and high gas hydrate saturation occur, associated with a marked increase in electrical resistivity and *P* wave velocity [*Riedel et al*., 2006]. Despite the presence of gas hydrate, which is believed to increase sediment strength [e.g., *Waite et al*., 2009; *Priest et al*., 2014], breakouts are also observed across the massive gas hydrate cap from 30 to 50 mbsf at Site U1328. The magnitude of the horizontal stresses acting in this interval must exceed the

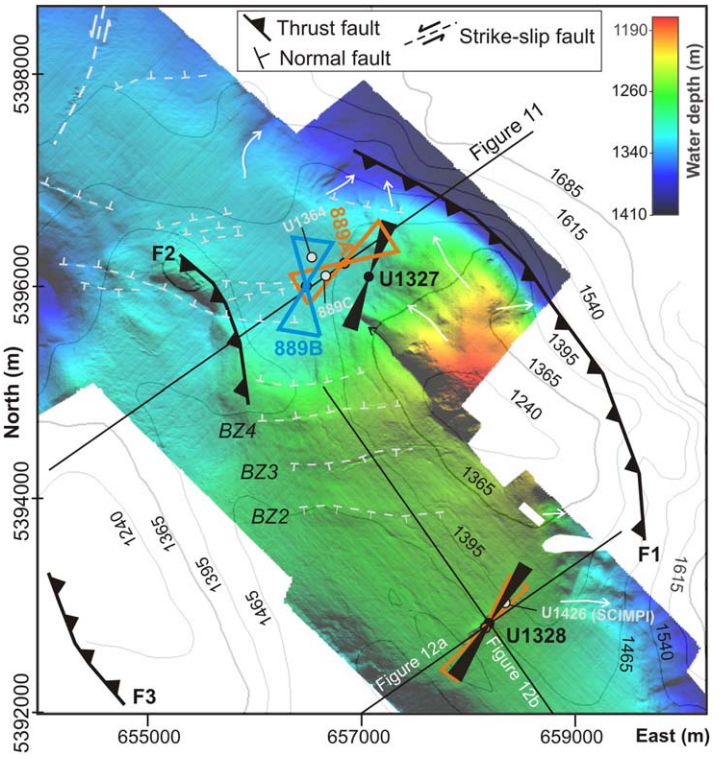

Figure 10. Map of the central portion of the IODP Expedition 311 transect around Sites U1327, U1328, and ODP Site 889. The orientation of S_{Hmax} derived from borehole breakouts at these sites is shown at each borehole (compare to Figure 6 and Table 1). Seafloor depth from AUV mapping [*Paull et al.*, 2015] is shown underlain with contours of depth (in meter below sea surface) to the top of accreted sediments. Small faults within slope sediments are marked with grey dashed lines (developed further after *Riedel et al.* [2002, 2010] and *Furlong* [2013]). The location of major thrust faults F1–F3 were inferred from seismic data (see Figure 11) as well as seafloor bathymetry (after *Westbrook et al.* [1994] and *Riedel et al.* [2002]). Slope failures are marked by white arrows.

strength of these hydrate-bearing sediments. No sediment sample from collected during X311 has been stress tested to date. Using sediment cores available at the IODP core repository and growing synthetic gas hydrate could be an alternative experiment to obtain sediment shear strength measurements; however, artificially formed gas hydrate in remolded sediments may strongly alter the resulting sediment physical properties [*Waite et al.*, 2009; *Priest et al.*, 2014]. We therefore have not undertaken such experiments or extrapolated values from other experiments using sediments from other continental margins.

5.2. S_{Hmax} Directions and Prism Deformation

Comparing the direction of measured maximum horizontal stress to the structural setting of the accreted prism generally yields a good correlation with the plate convergence direction of ~49° [from *DeMets et al.*, 2010] and is consistent with the orientation of accreted ridges and underlying thrust faults which are the primary structural expressions of tectonic compression (Figure 14). The seafloor multibeam bathymetry of the region shows that the accreted ridges along the deformation front systematically switch orientation, which may impact local stress orientation. Ridge and thrust fault segments a few kilometers in length consistently appear from west of the deformation front to east of the shelf-edge. Structural lineaments of individual ridge segments are oriented ~110° ± 10° and ~150° ± 10° [*Riedel et al.*, 2016], subperpendicular to the direction of relative plate motion (Figure 15). Most obvious at Site U1326 (Figure 7), the fact that our observed S_{Hmax} is not in the plate convergence direction may be due to the orientation and rotation of these ridge segments.

Breakout orientation in the central portion of the X311 drilling transect at Sites U1327 and U1328 is consistent with the overall trend of the subducting plate motion, underlying tectonic structures, and distribution of the accreted sediments (Figure 10). Results from wireline logging at Site 889, however, reveal a slightly different orientation of S_{Hmax}. Figure 10 illustrates the location of numerous normal faults around Site 889 and U1327 which shows the complex interplay of various forces that act on the boreholes. The normal faults are only seen within the seismically well-layered slope-sediment cover and are undetectable in the underlying accreted sediments that lack seismic coherency. Because the wireline logs in Holes 889A and 889B were obtained from depths >100 mbsf, the breakouts identified occur exclusively within the accreted complex. The time lag between drilling and logging does not affect the orientation of the breakouts [*Moore et al.*, 2011], and thus, the operational differences between the LWD and wireline data are not responsible for the different orientations in S_{Hmax}. Structural analyses of recovered core was completed for Site 889 (not for cores from X311) and the conclusion from analyses of deformation features in the recovered sediments from Holes 889A and 889B at depths where breakouts are observed (>100 mbsf) stated that "pervasive

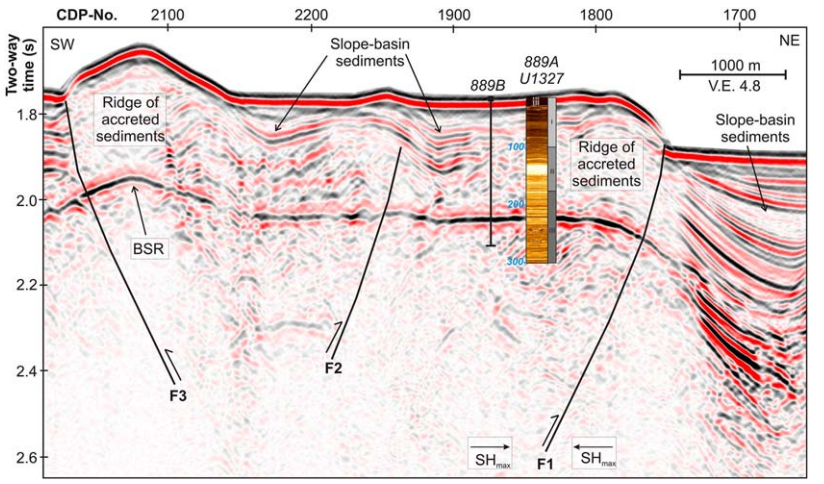

Figure 11. Section of seismic line 8908 across drill sites 889 and U1327 showing difference in seismic character of accreted and slope-basin sediments, as well as location of major thrust faults (see Figure 10 for location). Lithological units defined from Site U1327 are shown next to the LWD image. Units II and III are within the accreted sediment complex, whereas Unit I is formed by the well-stratified slope-basin sediments.

fracturing is indicative of bulk distributed strain" [*Westbrook et al*., 1994]. This strain may have developed as sediments were moved up through the hanging wall of the underlying thrust fault (F1 in Figures 10 and 11). Whether rotation of local fault-blocks (as suggested from the shallower normal faults) or accumulated stress within the accreted sediments causes the variation of S_{Hmax} orientation over such short lateral distances between these three boreholes (~500 m) is not resolvable from the data available. The direction of S_{Hmax} and large uncertainty in these wireline data is thus reasonably consistent with the results from the other holes across the transect (U1326, U1327, U1328, and U1329).

An exception from the margin-normal trend in S_{Hmax} is clearly observed at Site U1325, where S_{Hmax} (~98°) is rotated clockwise from the dominant subduction direction. Site U1325 lies within a slope basin between two major thrust faults and subsidence in response to neighboring thrust faults creates a catchment for downslope turbidite sedimentation. The borehole breakout orientation, S_{hmin}, is nearly N-S and may reflect the extensional nature of this bowl-shaped slope basin. As seen in the seismic image (Figure 9b), this basin is also wedged between smaller-scale ridges where infilling sediments are continuously deforming. The breakout orientation thus reflects a complex and composite stress field that amalgamates various local stress components and does not simply align with the nearby thrust faults in the subduction direction.

Borehole breakout analyses in other convergent margin settings show similar margin-parallel S_{Hmax} directions. In particular, whereas most sites drilled in the Nankai Trough show a margin-perpendicular S_{Hmax} orientation, S_{Hmax} is margin-parallel in a Kumano fore-arc basin site [*Chang et al*., 2010; *Lin et al*., 2010]. One out of three sites along the Costa Rica subduction zone indicates margin-parallel S_{Hmax} from breakouts, and here the variability in S_{Hmax} orientation has been attributed to the effects of a network of normal faults that subdivide the sediment cover into a number of independently deforming blocks [*Malinverno et al*., 2016].

5.3. The Regional Stress Field

In the onshore area of the Cascadia subduction zone, the maximum compressive stress (σ_1) is horizontal and is oriented roughly parallel with the strike of the margin [*Mulder*, 1995; *Wang et al*., 1995; *Wang and He*, 1999; *Balfour et al*., 2011]. This margin-parallel compression is in sharp contrast with the margin-normal direction of fastest crustal shortening observed with geodetic measurements [e.g., *Balfour et al*., 2011; *Mazzotti et al*., 2011]. The geodetic shortening, however, only reflects elastic stress changes due to current interseismic locking of the megathrust and cannot be used to constrain the orientation of absolute principal stresses [*Wang*, 2000].

The onshore margin-normal compressive stress has a similar magnitude to the vertical stress [*Wang et al*., 1995]. *Wang and He* [1999] explain that the relative magnitudes of the margin-normal and vertical stresses in the inner fore-arc are controlled by two competing effects: gravity, which in the presence of margin

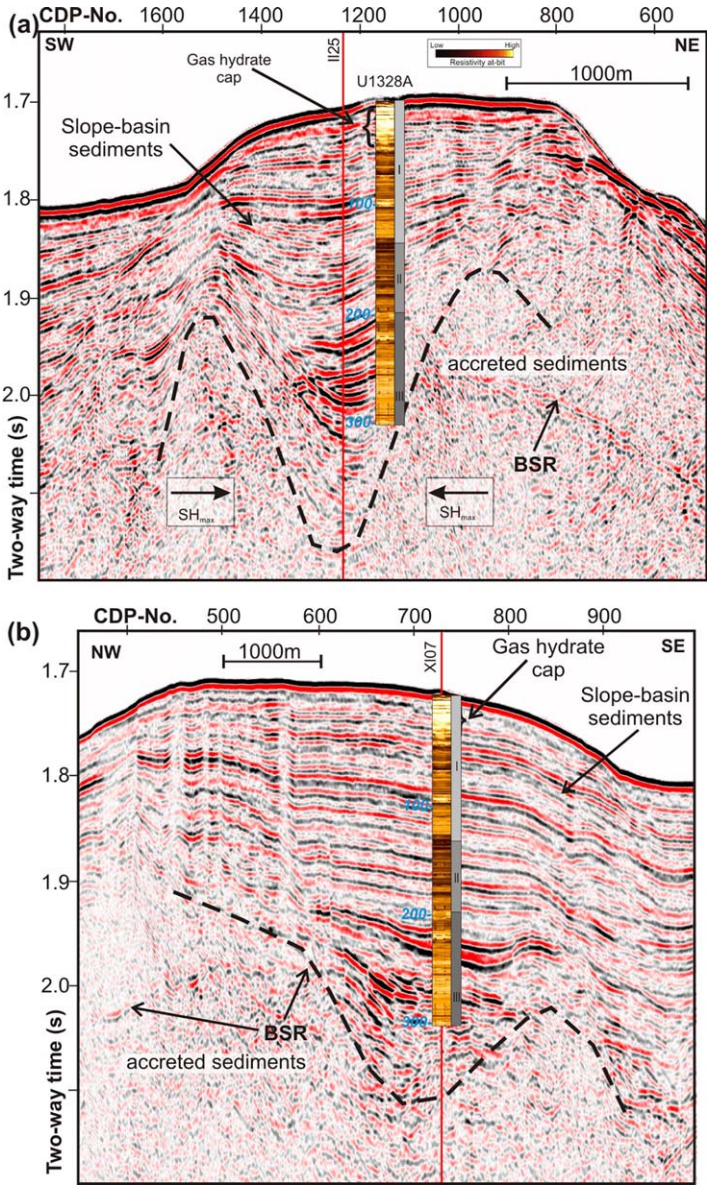

Figure 12. Two perpendicular seismic sections across Site U1328 (Bullseye Vent) showing the structural setting of a bowl-shaped basin of well-laminated slope sediments overlying sediments of the accreted prism of low seismic amplitude. Locations of these lines see Figure 10. (a) Line XL07 is parallel to the orientation of maximum horizontal compression (S_{Hmax}). The buried folds of accreted sediments are being compressed and in turn deform the slope sediments into a bowl-shaped basin. (b) Line IL25 shows the development of additional vents (vertical low amplitude structures) to the NW of Bullseye vent [*Riedel et al.*, 2002]. Also shown on the seismic images are the RAB data depicting the gas hydrate cap within the uppermost ~35 mbsf.

topography promotes greater vertical stress, and plate coupling, which promotes greater margin-normal stress. The observed "neutral" state of stress reflects the fact that the weak subduction megathrust barely provides enough lateral compression to prevent the inner fore arc from collapsing under its own weight [*Wang and He*, 1999].

For the offshore area, however, *Wang and He* [1999] show that the plate coupling effect dominates. The presence of active fold-and-thrust structures indicates that margin-normal compression comprises the maximum stress in the outer accretionary wedge over geological timescales. Therefore, the direction of maximum compression rotates from margin-normal in the frontal prism to margin-parallel in the inner fore arc. Crustal earthquakes along the southwest coast of Vancouver Island may suggest that margin-normal compression prevails from the deformation front all the way to the coast at the present time [*Balfour et al.*, 2011].

Although the long-term state of stress in the outer wedge is dominated by margin-normal compression as is evidenced by the fold-and-thrust structures, it remains unclear how the stresses fluctuate throughout great megathrust earthquake cycles. Using the Nankai accretionary margin as a primary example, *Wang and Hu* [2006] proposed that the outer wedge may undergo large subhorizontal compression during a great earthquake because of a velocity-strengthening behavior of the shallow segment of the megathrust. Their dynamic Coulomb wedge model predicts that during the interseismic phase when the seismogenic zone further downdip is locked, the outer wedge becomes increasingly relaxed until it is dominated by the gravity effect, a prediction that appears to gain support from stress observations from the Nankai margin [*Lin et al.*, 2015]. In order to know whether the outer prism is presently in a compressed or relaxed state, we need to compare the relative magnitude of S_{Hmax} with that of the vertical stress S_V. Our borehole breakout results clearly indicate that S_{Hmax} is generally margin-normal, but we unfortunately do not know how its magnitude compares with S_V.

Estimating the magnitude of S_{Hmax} (and S_{hmin} for that matter) requires both the observed widths of borehole breakouts (WOBs) and laboratory-derived unconfined compressive strengths (UCSs) of the sediment [e.g.,

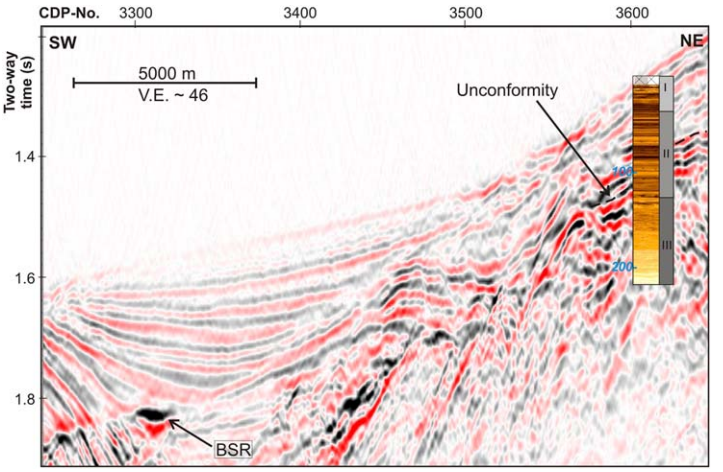

Figure 13. Section of MCS line 8908 across Site U1329. A BSR is observed to the SW of the drill site, whereas the seismic image at U1329 is complex due to an overlap of the depth of the base of the GHSZ and the unconformity.

Zoback et al., 2003; *Lin et al.*, 2013]. Although it may be possible to determine WOBs from our borehole data, we currently do not have independent measurements of UCSs on any sediment sample. *Chang et al.* [2006] and *Huffmann and Saffer* [2016] used empirical relationships to link *P* wave velocity and UCS in their study areas and computed a wide range of possible values for sediment compressive strength. The same approach cannot be readily applied to our study area, because the effects of gas hydrates above and free gas below the gas hydrate stability zone on *P* wave velocity can be significant and skew the assigned value of UCS. Furthermore, it is not well known how the *P* wave velocity relates to the actual value of UCS because additional factors such as gas hydrate structure at the pore-scale play a significant role on controlling sediment strength [e.g., *Waite et al.*, 2009; *Priest et al.*, 2014].

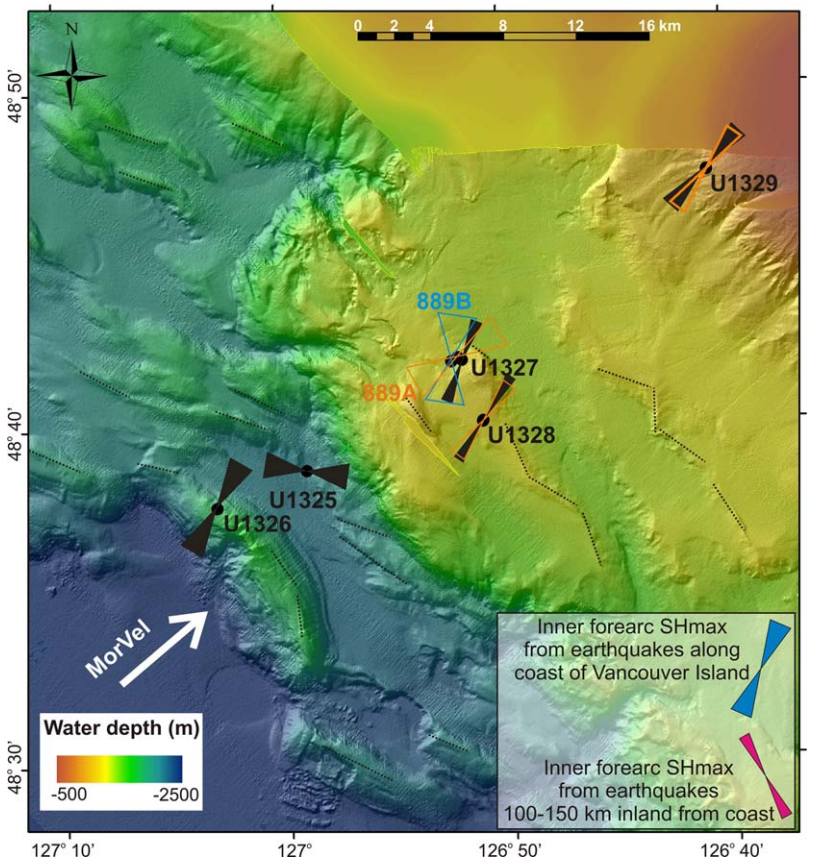

Figure 14. Composite map showing seafloor multibeam bathymetry, IODP Expedition 311 drilling transect (Sites U1325–U1329), and Site 889 from ODP Leg 146 with orientations of maximum compressive stress (same color-code as in Figure 6). The inset shows orientations of maximum compressive stress inferred from crustal earthquakes for the inner fore-arc region along the west coast of Vancouver Island (dark blue rosette symbol) from *Balfour et al.* [2011] and farther inland (magenta rosette symbol) from *Wang et al.* [1995]. Note also the apparent fragmentation of the deformation front and entire prism indicated by several representative line-segments (black dotted lines; for further details see *Riedel et al.* [2016]).

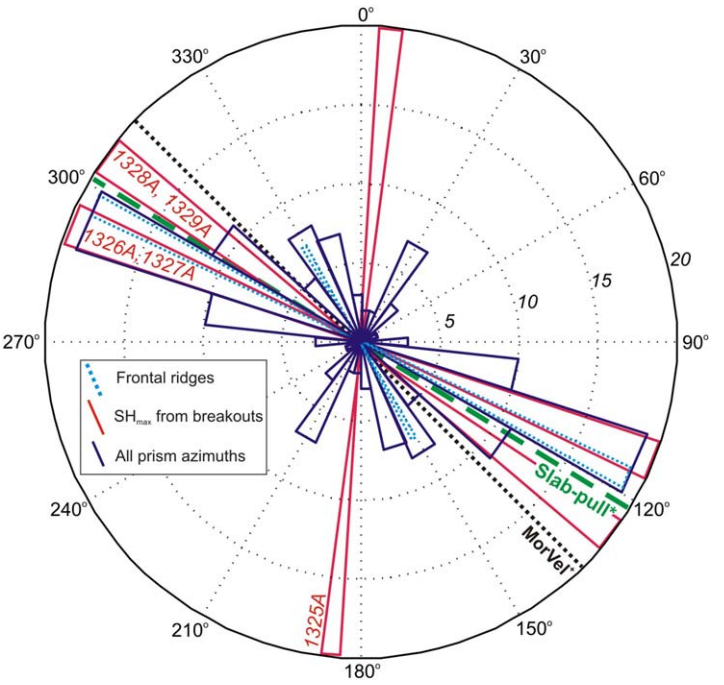

Figure 15. Rose diagram of strike orientations of digitized lineaments of accretionary ridges across the Northern Cascadia margin using high-resolution seafloor multibeam data (modified from *Riedel et al*. [2016]). Lengths of individual segments (binned at 5°) represent the number of occurrences of the individual strike angle. Orientations of maximum horizontal compression from breakouts are shown as red lines for all sites of IODP Expedition 311 (note, the length of these segments is not scaled by the number of occurrences). Orientations of tectonic forces in the region taken from the literature are rotated to represent their strike orientation (+90°): MorVel vector [*DeMets et al*., 2010] as main subduction orientation (black dotted line), and slab pull (green dashed line) taken from *Wang et al*., [1997] for the region of the central accretionary prism off Vancouver Island.

Cascadia is presently at a rather late stage of its interseismic phase [*Wang and Tréhu*, 2016]. Knowing the contemporary state of the stress in the outer wedge helps us understand the frictional behavior of the shallowest segment of the megathrust directly beneath. Depending on whether the prism is in a relaxed ($S_{Hmax} < S_V$) or compressed state ($S_{Hmax} > S_V$), we could infer whether the shallow megathrust exhibits a velocity-strengthening or velocity-weakening behavior, respectively [*Wang and Hu*, 2006]. Because of the young age of the subducting plate and the thick sedimentary cap on top of it, the shallow megathrust in Cascadia is very warm, making many of the velocity-strengthening clay minerals unstable. It thus may exhibit velocity-weakening [*Hyndman and Wang*, 1993] and stay locked during the interseismic phase, so that the overlying outer prism does not relax. If so, there is a higher likelihood that coseismic rupture could extend near the deformation front and enhance tsunami generation, similar to the trench-breaching rupture during the 2011 Mw = 9 Tohoku-oki earthquake [*Kodaira et al*., 2012]. Our findings of persistently margin-normal orientation of S_{Hmax} are consistent with this notion, although they do not prove it because we do not know whether $S_{Hmax} > S_V$ at the present time.

6. Summary and Conclusions

We have determined the orientation of maximum horizontal stress from borehole breakouts using logging-while-drilling data acquired during IODP Expedition 311 in a transect drilled across the northern Cascadia margin. To complement the structural analyses, we have utilized wireline logging data acquired at two sites in the transect during IODP Expedition 311 and at Site 889 during ODP Leg 146, obtaining breakout orientations in a total of seven drill sites. The breakouts reveal orientations of the maximum horizontal compressive stress (S_{Hmax}) that are consistent with the margin's subduction setting. With the exception of Site U1325 within a slope-basin (just landward of the first accretionary ridge) all breakouts suggest a relatively uniform NE-SW orientation of S_{Hmax}.

The observed breakout orientations indicate clearly that the maximum horizontal compressive stress is oriented in the margin-normal direction in the outer accretionary wedge. If the magnitude of this compressive stress is greater than that of the vertical stress, it may reflect a velocity-weakening behavior and current locking of the shallow megathrust, which in turn, may suggests that a future megathrust earthquake may extend to near the deformation front and initiate a trench-breaching, tsumanigenic rupture. Our results thus provide strong motivation to determine the magnitude of this margin-normal compressive stress relative to the vertical stress. This requires direct measurements of the sediment compressive strength and other geotechnical properties that are currently unavailable.

The local compressive regime and underlying thrust tectonics of individual fault segments can also influence the breakout orientations. The deformation front itself is segmented, with prominent right-lateral strike-slip faults occurring at the intersection of individual segments. Accretionary ridges strike at two dominant orientations of ~120° (±10°) and ~150° (±10°). The majority of S_{Hmax} orientations follow the trend of fault segments and accretionary ridges striking at ~120°, with one site (889A) following the trend of ridge orientations striking ~150°. S_{Hmax} is oriented nearly parallel to the trend of accretionary ridges in a slope basin site (U1325). From these measurements of stress orientation in the outer accretionary wedge, we conclude that persistent margin-normal compression exists in direction of plate convergence along the deformation front of northern Cascadia subduction zone.

Acknowledgments

Samples and data were provided by the Integrated Ocean Drilling Program (IODP), and its predecessors, funded by the U.S. National Science Foundation and participating countries. Data from IODP Expedition 311 can be found online at the proceedings (http://publications.iodp.org/proceedings/311/311toc.htm#Expedition_research_results). Logging data from IODP/ODP Sites used in this study can be further accessed through the database of the Lamont Doherty Earth Observatory (http://iodp.ldeo.columbia.edu/DATA/). We thank the captain and crew of the R/V *JOIDES Resolution* and the technical staff for their support at sea during IODP Expedition 311 and ODP Leg 146. Additional thanks goes to the onboard science teams and post cruise scientific community, as well as Trevor Williams and Cristina Broglia (Lamont Doherty Earth Observatory), who postprocessed the LWD and wireline data from Expedition 311 and Leg 146. Maria Jose Jurado and an anonymous reviewer provided insightful comments that improved the paper.

References

Akiba, F., Y. Inoue, M. Saito-Kato, and J. W. Pohlman (2009), Data report: Diatom and foraminiferal assemblages in Pleistocene turbidite sediments from the Cascadia margin (IODP Expedition 311), northeast Pacific, in *Proceedings of Integrated Ocean Drilling Program 311*, edited by M. Riedel, T. S. Collett, M. J. Malone, and the Expedition 311 Scientists, Integrated Ocean Drill. Program Manage. Int., Inc., Washington, D. C., doi:10.2204/iodp.proc.311.211.2009.

Balfour, N. J., J. F. Cassidy, S. E. Dosso, and S. Mazzotti (2011), Mapping crustal stress and strain in southwest British Columbia, *J. Geophys. Res.*, *116*, B03314, doi:10.1029/2010JB008003.

Bell, J. S., and D. I. Gough (1979), Northeast-southwest compressive stress in Alberta: Evidence from oil wells, *Earth Planet. Sci. Lett.*, *45*, 475–482.

Chang, C., M. D. Zoback, and A. Khaksar (2006), Empirical relations between rock strength and physical properties in sedimentary rocks, *J. Pet. Sci. Eng.*, *51*, 223–237.

Chang, C., L. C. McNeill, J. C. Moore, W. Lin, M. Conin, and Y. Yamada (2010), In situ stress state in the Nankai accretionary wedge estimated from borehole wall failures, *Geochem. Geophys. Geosyst.*, *11*, Q0AD04, doi:10.1029/2010GC003261.

Davis, E. E., and R. D. Hyndman (1989), Accretion and recent deformation of sediments along the northern Cascadia subduction zone, *Geol. Soc. Am. Bull.*, *101*, 1465–1480.

Davis, E. E., R. D. Hyndman, and H. Villinger (1990), Rates of fluid expulsion across the northern Cascadia accretionary prism: Constraints from new heat flow and multichannel seismic reflection data, *J. Geophys. Res.*, *95*(B6), 8869–8889.

DeMets, C., R. G. Gordon, and D. F. Argus (2010), Geologically current plate motions, *Geophys. J. Int.*, *181*, 1–80, doi:10.1111/j.1365-246X.2009.04491.x.

Furlong, J. (2013), Characteristic morphology, backscatter, and sub-seafloor structures of cold vents on the northern Cascadia margin from high-resolution autonomous underwater vehicle data, MSc thesis, 181 pp., Univ. of Victoria, Victoria, B. C., Canada.

Goldberg, D., and A. Janik (2006), Data report: Stress orientation in gas hydrate-bearing sediments near Hydrate Ridge: Evidence from borehole breakouts observed from logging-while-drilling resistivity images, in *Proceedings of Ocean Drilling Program Scientific Results*, edited by A. M. Tréhu, et al., vol. 204, pp. 1–14, U.S. Gov. Print. Off., Washington, D. C. [Available at http://www-odp.tamu.edu/publications/204_SR/VOLUME/108.PDF.]

Hamilton, T. S., R. J. Enkin, M. Riedel, G. C. Rogers, J. W. Pohlman, and H. M. Benway (2015), Slipstream: An early Holocene slump and turbidite record from the frontal ridge of the Cascadia accretionary wedge off western Canada and paleoseismic implications, *Can. J. Earth Sci.*, *52*, 405–430.

Huffmann, K. A., and D. M. Saffer (2016), In situ stress magnitudes at the toe of the Nankai Trough accretionary prism, offshore Shikoku Island, Japan, *J. Geophys. Res. Solid Earth*, *121*, 1202–1217, doi:10.1002/2015JB012415.

Hyndman, R. D., and E. E. Davis (1992), A mechanism for the formation of methane hydrate and seafloor bottom-simulating reflectors by vertical fluid expulsion, *J. Geophys. Res.*, *97*, 7125–7041.

Hyndman, R. D., and K. Wang (1993), Thermal constraints on the zone of major thrust earthquake failure: The Cascadia subduction zone, *J. Geophys. Res.*, *98*(B2), 2039–2060.

Hyndman, R. D., K. Wang, T. Yuan, and G. D. Spence (1993), Tectonic sediment thickening, fluid expulsion, and the thermal regime of subduction zone accretionary prisms: The Cascadia margin off Vancouver Island, *J. Geophys. Res.*, *98*(B12), 21,865–21,876.

Hyndman, R. D., G. D. Spence, N. R. Chapman, M. Riedel, and R. N. Edwards (2001), Geophysical studies of marine gas hydrate in northern Cascadia, in *Natural Gas Hydrates, Occurrence, Distribution and Detection, Geophys. Monogr.*, vol. 124, edited by C. K. Paull and W. P. Dillon, pp. 273–295, AGU, Washington, D. C.

Kastner, M., K. A. Kvenvolden, M. J. Whiticar, A. Camerlenghi, and T. D. Lorenson (1995), Relation between pore fluid chemistry and gas hydrate associated with bottom-simulating reflectors at the Cascadia margin, Sites 889 and 892, in *Proceedings of Ocean Drilling Program Scientific Results*, vol. 146, Part 1, pp. 175–187, Ocean Drill. Program, College Station, Tex.

Kodaira, S., T. No, Y. Nakamura, T. Fujiwara, Y. Kaiho, S. Miura, N. Takahashi, Y. Kaneda, and A. Taira (2012), Coseismic fault rupture at the trench axis during the 2011 Tohoku-oki earthquake, *Nature Geosci.*, *5*, 646–650, doi:10.1038/ngeo1547.

Lay, T., et al. (2005), The great Sumatra-Andaman earthquake of 26 December 2004, *Science*, *308*, 1127–1133.

Lin, W., et al. (2010), Present-day principal horizontal stress orientations in the Kumano forearc basin of the southwest Japan subduction zone determined from IODP NanTroSEIZE drilling Site C0009, *Geophys. Res. Lett.*, *37*, L13303, doi:10.1029/2010GL043158.

Lin, W., M. Conin, J. C. Moore, F. M. Chester, Y. Nakamura, J. J. Mori, L. Anderson, E. E. Brodsky, H. Eguchi, and Expedition 343 Scientists (2013), Stress state in the largest displacement area of the 2011 Tohoku-Oki earthquake, *Science*, *339*(6120), 687–690, doi:10.1126/science.1229379.

Lin, W., et al. (2015), Distribution of stress state in the Nankai subduction zone, southwest Japan and a comparison with Japan Trench, *Tectonophysics*, doi:10.1016/j.tecto.2015.05.008, in press.

Lopez, C., G. D. Spence, R. D. Hyndman, and D. Kelley (2010), Frontal ridge slope failure at the northern Cascadia margin: Margin-normal fault and gas hydrate control, *Geology*, *38*(11), 967–970.

Malinverno, A., M. Kastner, M. E. Torres, and U. G. Wortmann (2008), Gas hydrate occurrence from pore water chlorinity and downhole logs in a transect across the northern Cascadia margin (Integrated Ocean Drilling Program Expedition 311), *J. Geophys. Res.*, *113*, B08103, doi:10.1029/2008JB005702.

Malinverno, A., S. Saito, and P. Vannucchi (2016), Horizontal principal stress orientation in the Costa Rica Seismogenesis Project (CRISP) transect from borehole breakouts, *Geochem. Geophys. Geosyst.*, *17*, 65–77, doi:10.1002/2015GC006092.

Mazzotti, S., L. J. Leonard, J. F. Cassidy, G. C. Rogers, and S. Halchuk (2011), Seismic hazard in western Canada from GPS strain rates vs. earthquake catalog, *J. Geophys. Res.*, *116*, B12310, doi:10.1029/2011JB008213.

McNeill, L. C., M. Ienaga, H. Tobin, S. Saito, D. Goldberg, J. C. Moore, and H. Mikada (2004), Deformation and in situ stress in the Nankai Accretionary Prism from resistivity-at-bit images, ODP Leg 196, *Geophys. Res. Lett.*, *31*, L02602, doi:10.1029/2003GL018799.

Moore, J. C., C. Chang, L. McNeill, M. K. Thu, Y. Yamada, and G. Huftile (2011), Growth of borehole breakouts with time after drilling: Implications for state of stress, NanTroSEIZE transect, SW Japan, *Geochem. Geophys. Geosyst.*, *12*, Q04D09, doi:10.1029/2010GC003417.

Mulder, T. (1995), Small earthquakes in southwestern British Columbia (1975–1991), PhD thesis, Univ. of Victoria, Victoria, B. C., Canada.

Paull, C. K., D. W. Caress, H. Thomas, E. Lundsten, K. Anderson, R. Gwiazda, M. Riedel, M. McGann, and J. C. Herguera (2015), Seafloor geomorphic manifestations of gas venting and shallow sub bottom gas hydrate occurrences, *Geosphere*, *11*(2), 491–513, doi:10.1130/GES01012.1.

Plumb, R. A., and S. H. Hickman (1985), Stress-induced borehole elongation: A comparison between the four-arm dipmeter and the borehole televiewer in the Auburn geothermal well, *J. Geophys. Res.*, *90*(B7), 5513–5521.

Priest, J. A., C. R. I. Clayton, and E. V. L. Rees (2014), Potential impact of gas hydrate and its dissociation on strength of host sediment in the Krishna-Godavari Basin, *J. Mar. Pet. Geol.*, *58*(Part A), 187–198, doi:10.1016/j.marpetgeo.2014.05.008.

Rabinovich, A. B., and R. E. Thomson (2007), The 26 December 2004 Sumatra Zsunami: Analysis of tide gauge data from the World Ocean Part 1. Indian Ocean and South Africa, *Pure Appl. Geophys.*, *164*, 261–308, doi:10.1007/s00024-006-0164-5.

Riedel, M., G. D. Spence, N. R. Chapman, and R. D. Hyndman (2002), Seismic investigations of a vent field associated with gas hydrates, offshore Vancouver Island, *J. Geophys. Res.*, *107*(B9), 2200, doi:10.1029/2001JB000269.

Riedel, M., T. S. Collett, M. J. Malone, and the Expedition 311 Scientists (2006), *Proceeding of Integrated Ocean Drilling Program 311*, Integrated Ocean Drill. Program Manage. Int., Inc., Washington, D. C., doi:10.2204/iodp.proc.311.2006.

Riedel, M., E. C. Willoughby, N. Edwards, R. D. Hyndman, G. D. Spence, N. R. Chapman, M.-A. Chen, I. Novosel, and K. Schwalenberg (2009), Gas hydrate offshore Vancouver Island, northern Cascadia margin, in Natural Gas Hydrates—Energy Resource Potential and Associated Geologic Hazards, AAPG Mem., vol. 89, edited by T. Collett, A. Johnson, C. Knapp, and R. Boswell, pp. 433–450, American Association of Petroleum Geologists, Tulsa, Okla.

Riedel, M., T. S. Collett, and M. Malone (2010), Expedition 311 synthesis: Scientific findings, in *Proceedings of Integrated Ocean Drilling Program 311*, edited by M. Riedel, T. S. Collett, M. J. Malone, and the Expedition 311 Scientists, Integrated Ocean Drill. Program Manage. Int. Inc., Washington, D. C., doi:10.2204/iodp.proc.311.213.2010.

Riedel, M., K. Naegeli, and M. M. Côté (2016), Assessment of slope failures off Vancouver Island, *Geol. Surv. Can. Open File*, *8008*, 108 p., doi:10.4095/297904.

Scholz, N., M. Riedel, G. D. Spence, R. D. Hyndman, T. James, K. Naegeli, B. Dugan, J. W. Pohlman, and T. Hamilton (2011), Do dissociating gas hydrates play a role in triggering submarine slope failures? A case study from the Northern Cascadia margin, paper presented at Proceedings of the 7th International Conference on Gas Hydrates, ICGH, Edinburgh, U. K.

Tajima, F., J. Mori, and B. L. N. Kennett (2013), A review of the 2011 Tohoku-oki earthquake (Mw 9.0): Large-scale rupture across heterogeneous plate coupling, *Tectonophysics*, *586*, 15–34, doi:10.1016/j.tecto.2012.09.014.

Tingay, M., Reinecker, J., Müller, B. (2008), Borehole breakout and drilling-induced fracture analysis from image logs, in *The World Stress Map Project*, GFZ, German Research Centre for Geosciences, Potsdam, Germany. [Available at http://dc-app3-14.gfz-potsdam.de/pub/guidelines/WSM_analysis_guideline_breakout_image.pdf.]

Torres, M. E., et al. (2008), Methane hydrate formation in turbidite sediments of northern Cascadia, IODP Expedition 311, *Earth Planet. Sci. Lett.*, *271*, 170–180, doi:10.1016/j.epsl.2008.03.061.

Wada, I., S. Mazzotti, and K. Wang (2010), Intraslab stresses in the Cascadia subduction zone from inversion of earthquake focal mechanisms, *Bull. Seismol. Soc. Am.*, *100*(5a), 2002–2013, doi:10.1785/0120090349.

Waite, W. F., et al. (2009), Physical properties of hydrate-bearing sediments, *Rev. Geophys.*, *47*, RG4003, doi:10.1029/2008RG000279.

Wang, K. (2000), Stress-strain "paradox," plate coupling, and forearc seismicity at the Cascadia and Nankai subduction zones, *Tectonophysics*, *319*, 321–338.

Wang, K., and Y. Hu (2006), Accretionary prisms in subduction earthquake cycles: The theory of dynamic Coulomb wedge, *J. Geophys. Res.*, *111*, B06410, doi:10.1029/2005JB004094.

Wang, K., and J. He (1999), Mechanics of low-stress forearcs: Nankai and Cascadia, *J. Geophys. Res.*, *104*(B7), 15,191–15,205.

Wang, K., and J. He (2008), Effects of frictional behavior and geometry of subduction fault on coseismic seafloor deformation, *Bull. Seismol. Soc. Am.*, *98*, 571–579, doi:10.1785/0120070097.

Wang, K., and A. M. Tréhu (2016), Some outstanding issues in the study of great megathrust earthquakes—The Cascadia example, *J. Geodyn.*, *98*, 1–18, doi:10.1016/j.jog.2016.03.010.

Wang, K., T. Mulder, G. C. Rogers, and R. D. Hyndman (1995), Case for very low coupling stress on the Cascadia subduction fault, *J. Geophys. Res.*, *100*(B7), 12,907–12,918.

Wang, K., J. He, and E. E. Davis (1997), Transform push, oblique subduction resistance, and intraplate stress of the Juan de Fuca plate, *J. Geophys. Res.*, *102*(B1), 661–674.

Westbrook, G. K., B. Carson, and R. J. Musgrave (1994), Site 888, in *Proceedings of the Ocean Drilling Program Initial Reports*, vol. 146, Ocean Drill. Program, College Station, Tex.

Yuan, T., G. D. Spence, R. D. Hyndman, T. A. Minshull, and S. C. Singh (1999), Seismic velocity studies of a gas hydrate bottom-simulating reflector on the northern Cascadia continental margin: amplitude modeling and full waveform inversion, *J. Geophys. Res.*, *104*(B1), 1179–1192, doi:10.1029/1998JB900020.

Zoback, M. D., C. A. Barton, M. Brudy, D. A. Castillo, T. Finkbeiner, B. R. Grollimund, D. B. Moos, P. Peska, C. D. Ward, and D. J. Wiprut (2003), Determination of stress orientation and magnitude in deep wells, *Int. J. Rock Mech. Mining Sci.*, *40*, 1049–1076, doi:10.1016/j.ijrmms.2003.07.001.

Zoback, M. L. (1992), First- and second-order patterns of stress in the lithosphere: The World Stress Map project, *J. Geophys. Res.*, *97*(B8), 11,703–11,728.